

Palladium-based ferroelectrics and multiferroics: Theory and experimentShalini Kumari,¹ Dhiren K. Pradhan,¹ Nora Ortega,¹ Kallol Pradhan,¹ Christopher DeVreugd,² Gopalan Srinivasan,² Ashok Kumar,³ Tula R. Paudel,⁴ Evgeny Y. Tsybal,⁴ Alice M. Bumstead,⁵ J. F. Scott,^{5,*} and Ram S. Katiyar¹¹*Department of Physics and Institute for Functional Nanomaterials, University of Puerto Rico, San Juan, Puerto Rico 00931, USA*²*Physics Department, Oakland University, Rochester, Michigan 48309-4401, USA*³*Council of Scientific and Industrial Research (CSIR)-National Physical Laboratory, Dr. K. S. Krishnan Marg, New Delhi 110012, India*⁴*Department of Physics, University of Nebraska, Lincoln, Nebraska 68588-0299, USA*⁵*Department of Chemistry and Department of Physics, University of St. Andrews, St. Andrews KY16 8TJ, United Kingdom*

(Received 15 February 2017; revised manuscript received 27 April 2017; published 14 June 2017)

Palladium normally does not easily substitute for Ti or Zr in perovskite oxides. Moreover, Pd is not normally magnetic (but becomes ferromagnetic under applied uniaxial stress or electric fields). Despite these two great obstacles, we have succeeded in fabricating lead zirconate titanate with 30% Pd substitution. For 20:80 Zr:Ti, the ceramics are generally single-phase perovskites (>99%) but sometimes exhibit 1% PdO, which is magnetic at room temperature. The resulting material is multiferroic (ferroelectric-ferromagnetic) at room temperature. The processing is slightly unusual (>8 h in high-energy ball-milling in Zr balls), and the density functional theory provided shows that it occurs because of Pd⁴⁺ in the oversized Pb⁺² site; if all Pd⁴⁺ were to go into the Ti⁺⁴ perovskite *B* site, only a small moment of 0.1 Bohr magnetons would result.

DOI: [10.1103/PhysRevB.95.214109](https://doi.org/10.1103/PhysRevB.95.214109)**I. INTRODUCTION**

The discovery and analysis of large room-temperature magnetoelectric (ME) effects in single-phase material are among the aims of scientists working worldwide in the area of multiferroics (MFs), similar to the search for room-temperature superconductors. These systems require the presence of simultaneous ferroic order parameters with strong ME coupling for an increased number of logic states. During the last 15 years, the MF research communities have been searching for an alternative room-temperature MF material beyond BiFeO₃ (which has high leakage current) with large ME coupling for possible applications in high density electronic components and low heat dissipation memory and logic devices [1–8]. In the past few years, we have investigated several multicomponent systems, such as Pb(Zr,Ti)O₃(PZT)-Pb(Fe,Ta/Nb/W)O₃, and related family members, which have shown better ME effects compared to bismuth ferrite [9–12]. In a continuation of our search for larger ME effect, we have studied the Pb(Zr_{0.20}Ti_{0.80})_{0.70}Pd_{0.30}O_{3-δ} (PZTP30) system with an unusually large (30%) palladium occupancy in the *B* site of PZT. Our system is a simple tetragonal crystal structure with space group *P4mm*, as shown by x-ray diffraction (XRD) studies. This material exhibited a ME coupling coefficient ~0.36 mV/cm Oe (larger than most reported values for BiFeO₃ but about an order of magnitude lower than the highest reported [but unconfirmed] value of 7 mV/cm Oe for nanocrystalline BiFeO₃) [13]. This value is also an order of magnitude smaller than in cryogenic antiferromagnetic LiCoPO₄ or TbPO₄ or in ferromagnetic (FM) YIG (5.52, 6.62, and 5.41). For all BiFeO₃-based materials, the highest known ambient value is for the Bi₅Ti₃FeO₁₅ compound ($\alpha_{ME} \sim 10$ mV/cm Oe). In the case of (BiFeO₃)_{1-x}(BaTiO₃)_x and Bi_{1-x}Nd_xFeO₃ solid solutions, the maximum α_{ME} is of the order of 1 and

2.7 mV/cm Oe; therefore, our value is within an order of magnitude of that of the highest known ceramic [14].

The basic aim of this paper is to discriminate between two possible explanations of detailed data on ceramic PZTP30. First, is it a single-phase ferroelectric (FE) perovskite with Pd⁺² and Pd⁺⁴ substitutional at Pb *A* sites and Zr/Ti *B* sites, respectively, and a room-temperature MF? Or, second, is it merely a two-phase composite with FE PZT:Pd and a FM second phase?

A neutral Pd atom (Kr 4d [10]) has square planar complex, which gives zero magnetic moment ($\mu = 0$) and diamagnetism, but when it is in Pd⁺² or Pd⁺⁴ ionic states, it provides a large magnetic moment with outer shell configuration 4d⁸5s⁰ or 4d⁶5s⁰ with unpaired electrons in its *d* shell. Large electric fields can cause Pd to become FM [15–18]. The presence of Pd in PZTP30 has been confirmed by energy-dispersive x-ray spectroscopy (EDS), x-ray fluorescence spectroscopy (XRF), and x-ray photoemission spectroscopy (XPS) studies and assigned with related binding energies of Pd⁺² and Pd⁺⁴ ions as 336.37 eV, 342.9 eV, and 337.53 eV, 343.43 eV, respectively, which may be the origin of room-temperature magnetism in Pd substituted PZT ceramics. A sharp first-order FE phase transition was observed at ~569 K (± 5 K) for PZTP30, which is confirmed from dielectric and thermal analysis. Both FM and FE orderings with large ME are measured.

The basic physics and coupling mechanisms between spin and polarization in crystals, especially for single-phase ME systems, are not well studied yet for the next generation of logic and memory elements [19–23]. Due to the natural chemical incompatibility between magnetism and ferroelectricity in oxide perovskites, only a few single-phase MF oxides exist with sufficiently large magnitude of polarization and magnetization for real device applications. Some of the well-known potential MF materials are as follows: BiFeO₃, YMnO₃, Pb(Fe_{0.5}Nb_{0.5})O₃, Pb(Fe_{0.5}Ta_{0.5})O₃, Pb(Fe_{0.67}W_{0.33})O₃, TbMnO₃, etc. [8,12,24–26]. The most well-known room-temperature lead-free single-phase MF is BiFeO₃ (BFO), having both FE ($T_C = 1143$ K) and antiferromagnetic

*Author to whom correspondence should be addressed: jfs4@st-andrews.ac.uk

($T_N = 643$ K) phase transitions above room temperature; however, still it is not suitable for real practical device applications due to a high leakage current and the small ME coupling coefficient [27–30]. The MFs possess ferroic order parameters and cross coupling at cryogenic temperatures (either FE and/or magnetic transitions); among these the magnitude and directions of magnetic and FE orders often occur largely independent of each other. As a result, the ME coupling tends to be small [31–33]. The low operational temperatures (FE/FM), high leakage current, and/or weak ME coupling of most of the single-phase compounds have motivated researchers to continue the search for novel room-temperature ME MFs with larger ME coupling coefficients.

An alternate option is FE and FM composites/heterostructures, which have greater design flexibility for ME devices by combining FE and FM phases together; among them a heterostructure with FE/FM phases is the most popular design due to immense potential for high density logic states [34]. Single-phase ME materials with large ME coupling coefficients in ultrathin heterostructured films are important for tunnel junction-based devices, which can provide a higher degree of logic states under combined electric and magnetic control. These factors drive the endeavors for discovering new room-temperature single-phase MFs with giant ME coupling, beyond BiFeO₃. Several materials have recently been discovered, such as Pb(Zr_{0.53}Ti_{0.47})_{0.60}(Fe_{0.5}Ta_{0.5})_{0.40}O₃ (PZTFT) and the Bi-based Aurivillius oxides (Bi₅Ti₃Fe_{0.7}Co_{0.3}O₁₅), GaFeO₃, and LuFeO₃ [9,35–39].

Therefore, the discovery of an alternative room-temperature single-phase MF material is exciting. In this report, an attempt has been made to produce multiferroism and ME coupling at room temperature in PbZr_xTi_{1-x}O₃, which is known to be one of the best FE materials in nature, whereas palladium is a transition metal usually without any magnetic properties [40,41]. However, we have found multiferroicity (ferroelectricity and magnetism) with strong intrinsic ME coupling at room temperature in the palladium-substituted PZT.

II. EXPERIMENTAL DETAILS

Polycrystalline powder of Pb(Zr_{0.20}Ti_{0.80})_{0.70}Pd_{0.30}O_{3-δ} (PZTP30) was synthesized using a conventional solid-state reaction route from a stoichiometric mixture of highly pure (>99.99%) reagents PbO, ZrO₂, TiO₂, and PdO powders from Alfa Aesar. Mechanical ball milling of stoichiometric amounts of all ingredients was carried out in methanol with Zr balls (to avoid magnetic contamination), followed by calcination in air at 1150 °C for 8 h, using a Carbolite furnace (HTF1700) with a heating rate of 5 °C/min. This is a rather long time for a high-energy ball milling, and we believe that significant solid state chemistry occurred during the milling [42]. The synthesized phase-pure powder was pressed into pellets ($d = 13$ mm) at a uniaxial force of 5 tons and later sintered at 1200 °C for 8 h. Phase formations of the pellets were evaluated by x-ray diffractometer (Rigaku Ultima III) equipped with a CuK_α radiation source operating in the Bragg-Brentano geometry at 40 kV and 40 mA in a slow-scan mode 0.2°/min. The

Rietveld structure refinement was carried out using FullProf Suite software. Scanning electron microscopy (SEM) images were recorded at 5000× magnification with the help of a JEOL JSM-6480LV system operated with an accelerating voltage of 20 kV to study the surface morphology. The composition and valence states of the fabricated pellets were confirmed via XRF, EDS, and high-resolution XPS, correspondingly. The flat surface of the sintered pellets was polished with fine emery paper, and then top and bottom electrodes were made by coating high purity silver paint followed by heating at 200 °C for 2 h in air for better conduction and adhesion. The dielectric measurements were performed under vacuum (10⁻⁶ Torr) using an HP4294A impedance analyzer. Thermal control was achieved in the range of 200–700 K using a variable temperature microprobe system equipped with a programmable temperature controller (MMR Technologies, Inc.). The FE properties were measured using a Radiant RT 6000 high voltage system after poling the sample under a voltage of 1000 V for 6 h using a dc power supply (TREK, Inc., Model 677A) at room temperature. Low temperature magnetic properties of the PZTP30 samples were measured using a Quantum Design Physical Property Measurement System (PPMS) DynaCool in a wide range of temperature 25–300 K. The room-temperature ME measurements were carried out with a homemade ME setup using a magnet with a varying field of up to ±3 kOe with lock-in amplifier and reference ac magnetic field using a Helmholtz coil [43].

III. RESULTS AND DISCUSSION

A. Structural, microstructural, and elemental characterization

The Rietveld refinement of high-resolution XRD data provides straightforward and precise structural information. Detailed XRD studies have been performed on PZTP30 pellets used for magnetic and ME measurements with assumption of *A* site occupancy by Pb and *B* site by Zr, Ti, and Pd, with oxygen at the corner of BO₆ octahedral position. The Rietveld refinement of the diffraction patterns was performed by considering tetragonal *P4mm* symmetry [44,45]. The experimental and Rietveld simulated XRD patterns of PZTP30 bulk samples are shown in Fig. 1(a). The results demonstrated excellent fit, confirming pure tetragonal phase formation of the material belonging to the space group *P4mm*. The sharp Bragg peaks were assigned to their Miller indices with only a single very weak appearance of an extra reflection peaks that would be indicative of secondary phases and no peaks from lead-deficient pyrochlore phases. In particular, we do find PdO, which is magnetic at room temperature, but in amounts <1%, as shown by the XRD reflection at 34.2° in Fig. 1(b) [46,47]. The XRD are also known now for PbPdO₂, another magnetic palladium oxide at low temperature ($T < 90$ K), and although these are coincidentally hidden under the strongest PZT XRD lines, we find them at the 1% level in pure PbTiO₃ : Pd [48]. We refined many parameters, such as background, zero shift, specimen displacement, atomic positions, thermal factors, scale factor, lattice parameters, FWHM, and shape parameters. Pseudo-Voigt description of profile shape was taken into account as a profile setup for Rietveld refinement. The difference between the measured spectrum and the refined one

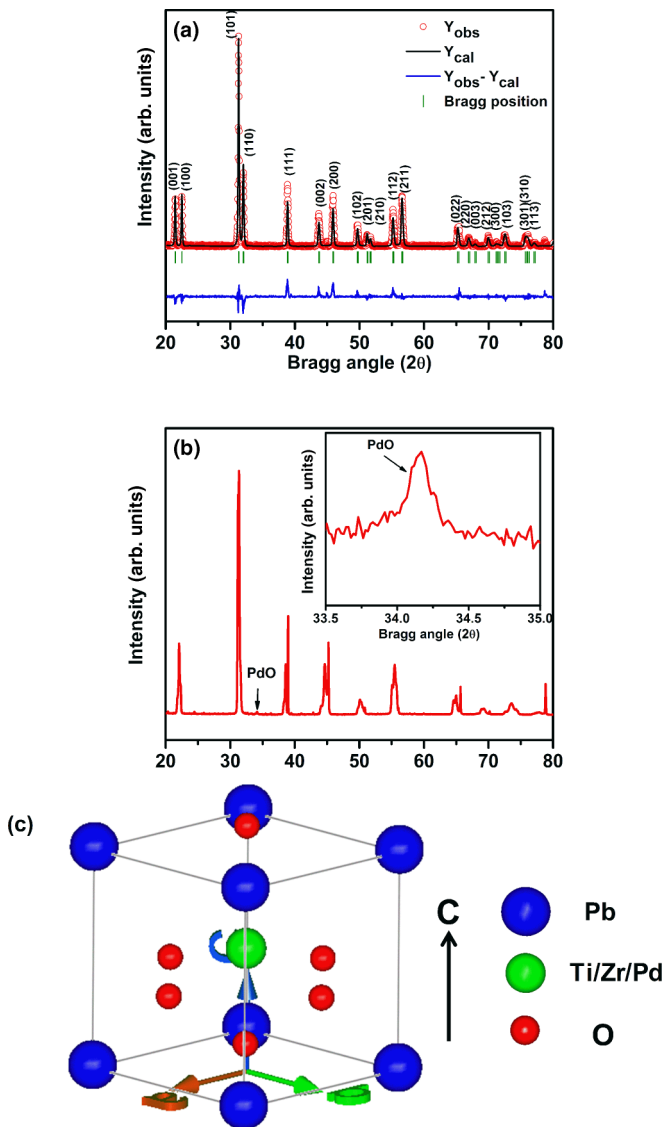


FIG. 1. (a) The Rietveld refined XRD patterns of PZTP30 ceramics using FullProf Suite software, (b) the presence of weak Bragg peak of PdO (<1%) and enlarged view in inset, and (c) the three-dimensional schematic sketch of the PZTP30 unit cell with tetragonal structure at room temperature.

is very small, and the reliability is ensured by the refinement parameters. All atoms were fixed to their site occupancies, as their variation did not appreciably affect the refinement results. During the refinement process, it was observed that reliability factors improve further when anisotropic thermal parameters were taken into account compared with the isotropic thermal parameters of the individual atoms. The crystal structure parameters and reliability factors obtained after XRD refinement are listed in Supplemental Material Tables S1 and S2 [49] and match well with the reported values for $\text{Pb}(\text{Zr}_{0.20}\text{Ti}_{0.80})\text{O}_3$ [44]. The calculated tetragonality ratio was $c/a = 1.047$, which indicates a preference for large polarization. Using the obtained unit cell parameters and atomic positions, a three-dimensional sketch of tetragonal PZTP30 unit cell projected along the c axis has been simulated,

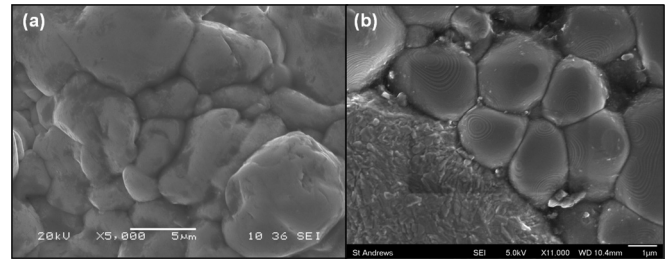


FIG. 2. The SEM micrographs of PZTP30 ceramic with 20:80% Zr/Ti, showing single-phase perovskite structure with terraced grains.

as shown in Fig. 1(c), which indicates that Pd was incorporated into the crystalline lattice of the PZT; hence the appearance of tetragonality in PZTP30 is consistent with PZT(20/80), the highly tetragonal Ti-rich version of PZT [44,45,50,51]. The bond lengths obtained after XRD refinement have been compiled in Supplemental Material Table S3 [49].

In any study of new MFs, it is essential to demonstrate that the magnetic and FE properties arise from a single chemical phase and that it is not a situation in which ferromagnetism originates from a second phase. To this end we have examined carefully via SEM the ceramic materials in this paper. The overall microstructure of PZTP30 pellets showed well-defined densely packed grains with average size ranging between ~ 3 – $10 \mu\text{m}$ surrounded by distinct grain boundaries, as shown in Fig. 2(a). The presence of different shapes and grain sizes with neck-to-neck compaction revealed that the grain growth process was almost completed during the sintering process. The Zr:Ti 20:80 specimens were mostly single-phase terraced perovskite [Fig. 2(b)]. The electron micrographs reveal three distinct grain structures: The largest in percentage and grain size have pseudo-hexagonal habitats; the second largest are rectilinear tetragonal; and there is a small percentage of a third phase (plus traces of Al, due to sintering in an alumina crucible). However, PdO in nanophase is FM above room temperature, and PbPdO_2 is also FM only below $T = 90 \text{ K}$ [46–48]. Since both are tetragonal, they are viable candidates for our tetragonal grains in the SEM micrographs of the 20:80 Zr/Ti specimens. This is discussed further below. However, without examination of the SEM data, we note that most of the Pd is Pd^{+4} , whereas the only two room-temperature magnetic phases anticipated as possible contaminants in this composite are PdO and PbPdO_2 , both of which are purely Pd^{+2} . PdO is weakly observed in the XRD data at $2\theta = 34.2^\circ$ but at <1% by weight. No XRD lines corresponding to the known diffraction pattern of PbPdO_2 are observed. The SEM data in Fig. 2 support our view that the 20:80 PZT is primarily (99%) single-phase perovskite. In a separate paper, we will present detailed studies of a second phase, identified as PbPdO_2 , which is magnetic below $T = 90 \text{ K}$; in $\text{PbTiO}_3 : \text{Pd}$ the XRD Bragg peaks happen to occur directly under those from PZT, so they are not visible in the present paper. We measure the atomic %, magnetic properties and perform transmission electron microscopy (TEM) studies of PbPdO_2 in that paper.

Some TEM data were also obtained. These have better resolution than the SEM and permit atomic percentages for

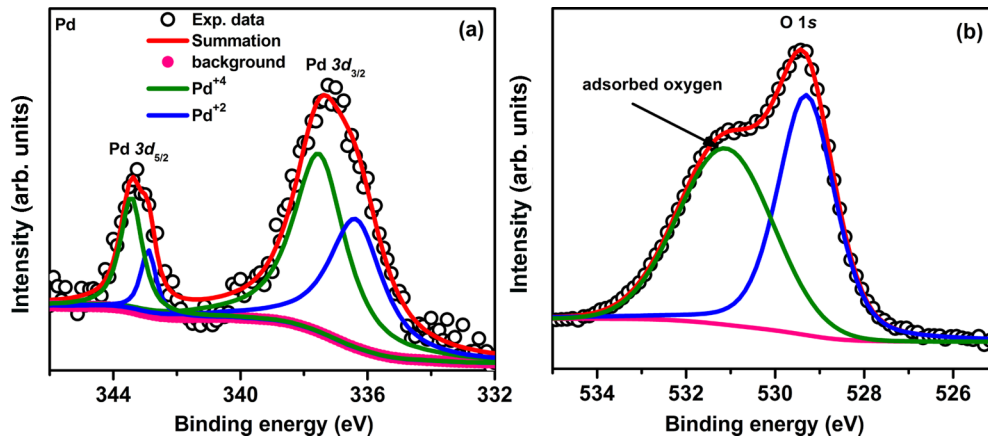


FIG. 3. (a) The XPS spectra of Pd $3d$ deconvoluted into two peaks; the binding energies at 336.37 eV, 342.9 eV and 337.53 eV, 343.43 eV are assigned to Pd^{2+} and Pd^{4+} , respectively. (b) The XPS spectra of O in PZTP30 ceramics at room temperature.

individual grains. These will be discussed further in a separate paper but support the conclusions here.

The presence of all elements in PZTP30 bulk was confirmed through XRF measurement. The average XRF data matched with the initial elemental compositions taken for this study within the experimental limitations (see Supplemental Material Table S4 [49]). The EDS data confirm that the ratio of Pd/Pb was generally somewhat higher than the intended 30%; this may arise from surface excess or from our theoretically based hypothesis that Pd goes into both the Ti^{4+} sites and the Pb^{2+} sites (see Supplemental Material S5 [49]).

For conclusive evidence of existence of all elements with their valence states, PZTP30 pellets were examined by high-resolution x-ray photoemission, spectroscopy (XPS). Figure 3 and the Supplemental Material S6 [49] show the core level high resolution XPS spectra of Pb $4f$, Zr $3d$, Ti $2p$, Pd $3d$, and O $1s$. The peak positions in the XPS spectra were referenced to C $1s$ peak at 284.8 eV. The observed binding energy positions of Pb are Pb $4f_{7/2}$ = 138.2 eV and Pb $4f_{5/2}$ = 143 eV, respectively. The high resolution XPS spectrum of Zr $3d$ and Ti $2p$ splits up into two components due to spin-orbit effects. The spin-orbit doublets of Zr and Ti were observed at the following binding energies: Zr $3d_{5/2}$ = 181.3 eV and Zr $3d_{3/2}$ = 183.7 eV; Ti $2p_{3/2}$ = 457.8 eV and Ti $2p_{1/2}$ = 463.5 eV. These energy values confirm the valence states of Zr^{4+} and Ti^{4+} ions without any trace of Ti^{3+} ions (which could in principle be responsible for some magnetism). Note that Pd^{4+} is an excellent fit in the B site because it and sixfold-coordinated Ti^{4+} have the same (0.061–0.062 nm) ionic radii. Pd^{2+} is too small to fit well in the Pb^{2+} site. The Pd $3d_{5/2}$ and Pd $3d_{3/2}$ doublets were deconvoluted into Pd^{2+} at binding energy 336.37 eV and 342.9 eV with Pd^{4+} at binding energy 337.53 eV and 343.43 eV, respectively, in PZTP30 ceramics [see Fig. 3(a)] [52]. Its effective area (occupied by Pd^{4+} ions) is quite large compared to Pd^{2+} ions (ratio: 4/3), which is the origin of magnetism in Pd-substituted PZT ceramics. The O $1s$ can be deconvoluted into two peaks with binding energies of 531.1 eV and 529.3 eV, with shallower binding energy peak belonging to the lattice oxygen and the deeper binding energy attributed to the surface adsorbed oxygen [see Fig. 3(b)] [53]. The binding energies for all the individual elements match the standard value [54].

Moreover, the presence of all elements in PZTP30 bulk was confirmed clearly through XPS measurement along with XRF measurement.

B. Dielectric and thermal studies

Temperature and frequency dependent dielectric studies were carried out over a wide range of temperatures and frequencies to understand the FE to paraelectric phase transition behavior and dielectric dispersion characteristic. The order and nature of the phase transition allows us to understand the domain dynamics above and below the Curie temperature (T_c). The variation of relative dielectric permittivity (ϵ_r) and loss tangent ($\tan \delta$) as a function of temperature at different frequencies for PZTP30 is shown in Fig. 4(a) and the inset, respectively. The dielectric permittivity decreases with increase in frequency for PZTP30, which is a signature of polar dielectrics. Here ϵ_r increases with increase in temperature, reaches a maximum, and then decreases. This observed sharp anomaly at ~ 569 K (± 5 K) represents the FE-paraelectric transition temperature (T_c). The dielectric permittivity further increases above ~ 600 K due to thermally activated charge carriers. (Note that T_c for undoped PZT at this 20:80 Zr/Ti ratio is ca. 720 K.) The temperature dependent $\tan \delta$ [inset of Fig. 4(a)] also shows an anomaly just below T_c above 1 kHz probe frequencies. At high temperatures, the value of $\tan \delta$ increases with a rise in temperature, which may be due to space charge polarization, and interfacial polarization across the Ag/PZTP30 interface. The substitution of Pd in PZT shifts the phase transition towards lower temperature. The observed T_c was further verified by differential scanning calorimetric (DSC) measurements, as shown in Fig. 4(b). The DSC curve indicates a sharp exothermic peak around 552 K (± 5 K), corresponding to FE-paraelectric phase transition temperature. The temperature for an exothermic peak in the DSC thermogram is nearly same as the FE phase transition temperature obtained from dielectric studies within the experimental uncertainty.

C. FE and FM properties

For the conclusive evidence of existence of ferroelectricity at room temperature, electrical polarization (P) versus electric field (E) hysteresis loop measurements have been carried out

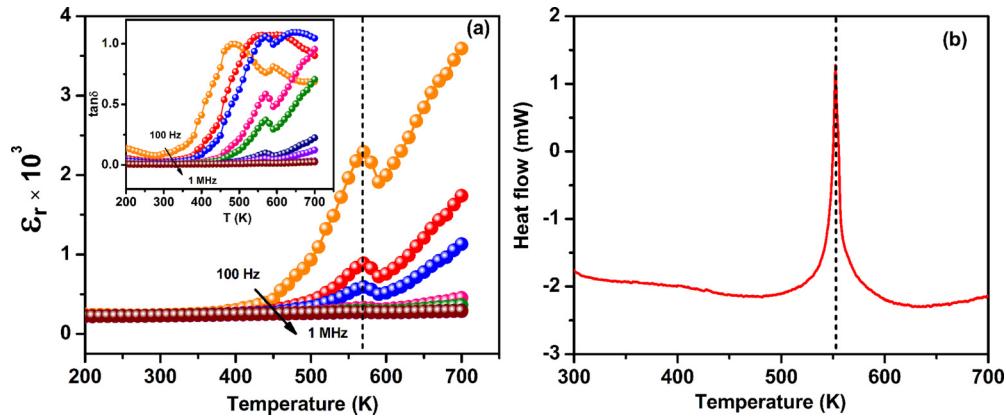


FIG. 4. (a) Temperature dependence of relative dielectric constant of PZTP30 ceramics at different frequencies; the inset shows respective temperature dependence of $\tan\delta$, (b) DSC thermogram of PZTP30 ceramics.

on PZTP30 samples at room temperature and are shown in Fig. 5(a). The P - E hysteresis loop measurements were performed on a poled ceramic sample. The coercive field (E_c), remanent polarization (P_r), and saturation polarization (P_s) are found to be 6.5 kV/cm, 10 $\mu\text{C}/\text{cm}^2$, and 16 $\mu\text{C}/\text{cm}^2$, respectively, with the maximum applied electric field (20 kV/cm). The presence of a saturated FE hysteresis loop confirms the presence of FE properties in PZTP30 ceramics.

Electrical hysteresis loops of PZTP30 ceramics were also measured using the positive-up negative-down (PUND) method before and after poling to determine the accurate remanent FE polarization (P_r). The PUND data provide switchable polarization (dP) \sim 6 $\mu\text{C}/\text{cm}^2$ and switchable remanent polarization (dP_r) \sim 5 $\mu\text{C}/\text{cm}^2$, respectively, as shown in Fig. 5(b), where the net switchable polarization (dP) is as follows:

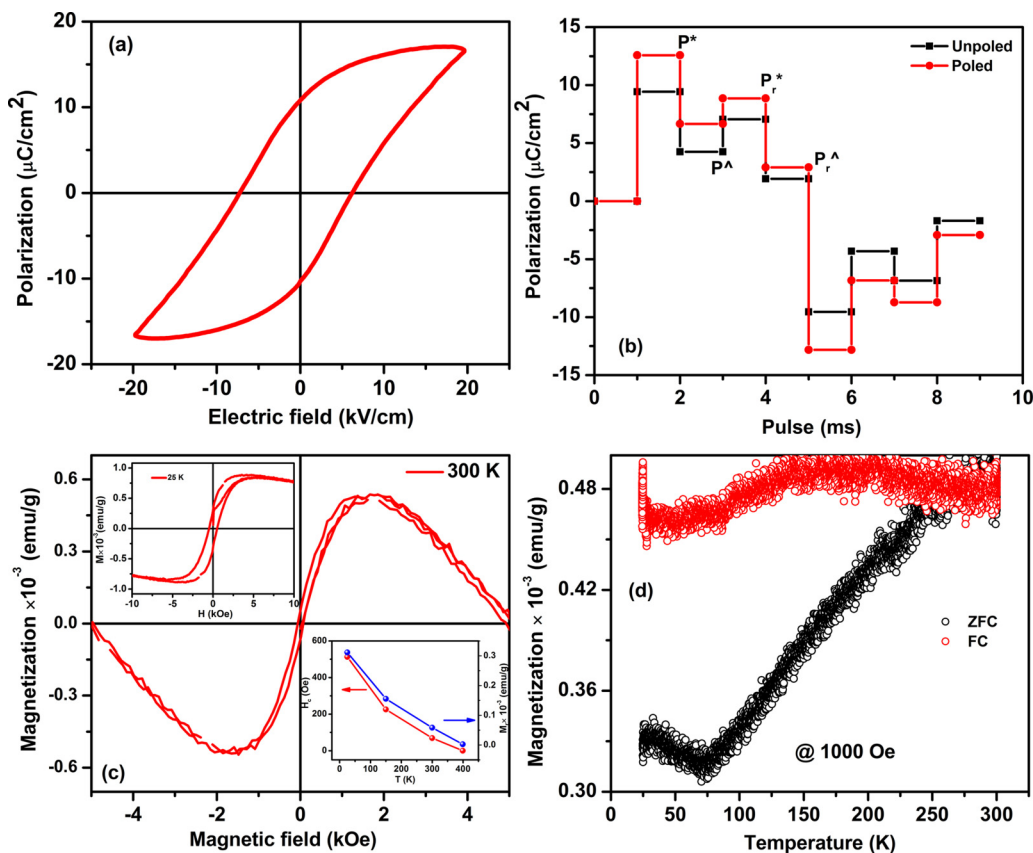


FIG. 5. (a) Ferroelectric (P - E) hysteresis loops of PZTP30 at room temperature. (b) PUND measurement of PZTP30 at room temperature. (c) Magnetic (M - H) hysteresis loops of PZTP30 at room temperature, M - H hysteresis loops of PZTP30 at 25 K (upper), and temperature dependence of H_c and M_r (lower) are in insets. (d) The ZFC and FC plot of PZTP30 ceramics at 1000 Oe.

$dP = P^* - P^\wedge$, where P^* = (total polarization) and P^\wedge = (nonswitchable polarization);

$dP_r = P_r^* - P_r^\wedge$, where P_r^* = (total remanent polarization) and P_r^\wedge = (nonswitchable remanent polarization).

The PUND data shown are not for the same specimen that was used for the hysteresis curve in Fig. 5(a) but for a leakier sample to show that even in that case the hysteresis is real ferroelectricity and not charge injection.

In order to prove the presence of magnetism and to understand the origin of magnetism in PZTP30, magnetization as a function of magnetic field at room temperature is depicted in Fig. 5(c). The Supplemental Material [Figs. S7(a)–S7(d)] [49] show the $M(H)$ hysteresis behavior performed at various temperatures. Standard PZT pellets were synthesized in same conditions as standards and do not show any magnetic ordering, whereas the Pd-doped PZT shows room-temperature well saturated $M-H$ curves with a large tail due to diamagnetic properties for higher applied magnetic field. Temperature-dependence of coercive field (H_c) and remanent magnetization (M_r) of PZTP30 is shown in the lower inset of Fig. 5(c), which monotonically increases with a decrease in temperature. Since no impurity phase at >1% level has been detected in the XRD patterns of PZTP30, the observed room-temperature magnetism could be due to the presence of $\text{Pd}^{2+}/\text{Pd}^{4+}$ ions into the host lattice, leading to the emergence of FM long-range ordering. In work on $(\text{PbTiO}_3 : \text{Pd})$ to be published separately, we see a distinct drop in $M(T)$ at 90 K, where a second phase (1% PbPdO_2) exhibits its FM-paramagnetic transition. Room-temperature ferromagnetism in some perovskite oxides have already been reported by substitution of FM particles such as Ni, Fe, and Co into the host lattice [55,56]. The presence of Pd^{2+} and Pd^{4+} states in PZTP30 is viewed by us as the origin of magnetism, and the existence of Pd^{2+} and Pd^{4+} states has been already confirmed from the XPS and XRF studies (Fig. 3 and Supplemental Material S4 [49]). The zero-field-cooled (ZFC) and field-cooled (FC) behavior of PZTP30 at 500 and 1000 Oe from 25 to 300 K has been plotted in the Supplemental Material [Fig. S7(e)] [49] and Fig. 5(d), respectively. The ZFC/FC data confirmed that there is no sharp transition up to 300 K. The results above prove that both FE and FM ordering exists above room temperature and hence room-temperature MF properties.

D. The ME properties

For further understanding of the MF nature, coupling between electric and magnetic order parameters in PZTP30 was investigated by studying the sample response to applied magnetic fields. The low-frequency ME voltage coefficients (α_{ME}) were measured. The sample was first poled at room temperature in an electric field of 30 kV/cm for 4 h. The ME measurement system consisted of an electromagnet for applying a bias magnetic field H , a pair of Helmholtz coils for applying an ac magnetic field δH , and lock-in detection for measuring the ME voltage δV generated across the sample thickness. The ME voltage was measured as a function of H for $H = 0\text{--}3\text{ kOe}$, an ac field $\delta H = 1\text{ Oe}$ at 100 Hz, and at room temperature. The measurements were performed for two field orientations: first, an in-plane mode for H and δH parallel to each other and to the sample plane (along direction 1) and perpendicular to δE along direction 3 (termed transverse

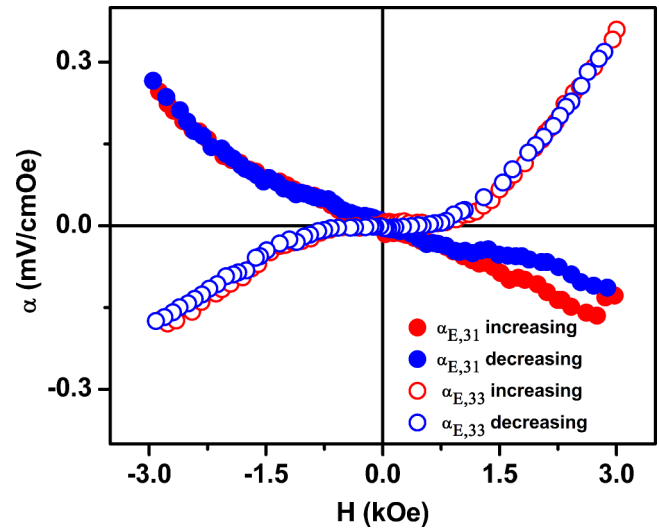


FIG. 6. Magnetolectric coupling coefficients (α_{E33} and α_{E31}) of PZTP30 ceramics as a function of an externally applied magnetic field H at room temperature.

orientation); second, an out-of-plane mode for all the three fields (H , δH , and δE) parallel to each other and perpendicular to the sample plane (all the fields along direction 3 and termed longitudinal orientation) [43]. The ME voltage coefficient $\alpha = \delta V / (t \delta H)$, where t is the sample thickness was estimated. The H dependence of longitudinal (α_{33}) and transverse (α_{31}) coupling coefficient for PZTP30 is plotted in Fig. 6.

Figure 6 shows representative data on bias magnetic field (H) dependence of transverse and longitudinal ME voltage coefficients. Consider first the results for the longitudinal field direction ($\alpha_{E,33}$). As H is increased, $\alpha_{E,33}$ remains small for $H < 0.7\text{ kOe}$, and then there is an increase in $\alpha_{E,33}$ with H to a maximum value of 0.36 mV/cm Oe at $H_m = 3\text{ kOe}$. Upon reversal of the direction of H , there is a sign reversal in $\alpha_{E,33}$ (a phase shift of 180°). The magnitude of $\alpha_{E,33}$ is small compared to values for positive fields and reaches a maximum of 0.18 mV/cm Oe, which is only 50% of the value for $+H$. This asymmetry in ME coefficient could be due to a magnetic anisotropy in the sample. The ME voltage coefficient versus H data do not show a peak or decrease to zero value for very high H due to saturation of magnetostriction. Similar observations were reported for several MF composites [57–60].

Figure 6 also shows α versus H data for the field parallel to the sample plane. The ME coefficient $\alpha_{E,31}$ shows a sign reversal relative to $\alpha_{E,33}$, and its magnitude increases almost linearly with H to a value of 0.15 mV/cm Oe. Upon reversal of direction of H , $\alpha_{E,31}$ becomes positive and shows a maximum value of 0.3 mV/cm Oe, which is twice the magnitude for $+H$. Since the ME voltage arises due to magnetic-mechanical-electrical interactions, the voltage coefficients are directly proportional to the product of piezoelectric (d) and piezomagnetic (q) coupling factors [58–60]. Since the parameter $q = d\lambda/dH$, where λ is the magnetostriction, the H dependence of α is expected to track the slope of λ versus H . Saturation of λ at high field leads to $\alpha_E = 0$. In this particular system, however, the data in Fig. 6 clearly indicate that saturation of λ does not happen

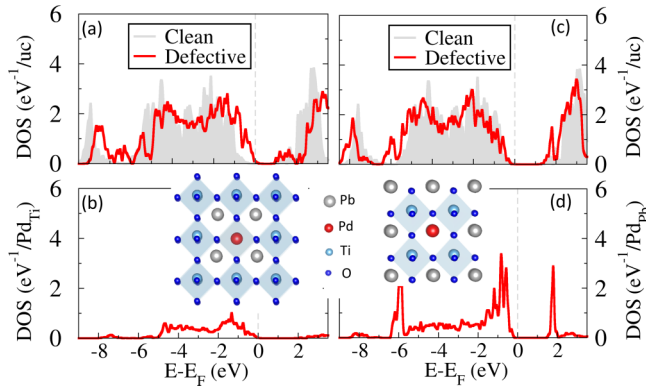


FIG. 7. DOS of clean (gray background) and defective (red curves) PbTiO_3 with a Pd atom replacing Ti (a) or Pb (c) in a $2 \times 2 \times 2$ PbTiO_3 supercell. The Fermi energy is shown by the dashed line. The DOS projected to the Pd atom replacing Ti (b) or Pb (d). The insets in (b) and (d) show the atomic structure of the supercell used in the calculations. In both cases, there is no exchange splitting of the spin bands, and the system remains nonmagnetic.

for $H = 3$ kOe. For most ferromagnets, the longitudinal (λ_L) and transverse (λ_T) magnetostrictions follow the relation $\lambda_L = 2\lambda_T$, and one expects $\alpha_{33} = 2\alpha_{E,31}$. Since the magnetization is rather small, any influence of the demagnetizing field on the magnetostriction and piezomagnetic coefficient will be negligible. One therefore anticipates $\alpha_{33} = 2\alpha_{E,31}$, as is the case for $+H$ in the data of Fig. 6. However, the data in Fig. 6 also show $\alpha_{31} \sim 2\alpha_{E,33}$ for $-H$. One needs to investigate the cause of asymmetry in α versus H data, which could be due to magnetocrystalline anisotropy field in the sample.

In the case of a bulk composite in which the magnetostrictive and the piezoelectric phases are uniformly mixed together, the transverse ME signal is formed by transverse magnetostriction, whereas the longitudinal ME signal is due to the longitudinal magnetostriction. For a majority of ferromagnets, the longitudinal magnetostriction is a factor of two higher than the transverse magnetostriction, and one expects $\alpha_L = 2\alpha_T$. Such an empirical relationship is confirmed in samples in the shape of cubes [61]. To measure both coefficients and to avoid the influence of demagnetizing fields, it is necessary to use long cylindrical samples. But such an approach also leads to other difficulties: high voltage required for polarization and mismatch of input impedance of the measuring device with the impedance of the sample. One possible solution is to measure $\alpha_{E,T}$ for a disk sample of a bulk composite and then estimate the longitudinal coefficient from the empirical relationship.

IV. THEORY

To understand the microscopic origin of magnetism in Pd-doped $\text{Pb}(\text{Zr}, \text{Ti})\text{O}_3$, we consider a Pd-doped PbTiO_3 (PTO) as a model system. Similar to $\text{Pb}(\text{Zr}, \text{Ti})\text{O}_3$, PTO is nonmagnetic and can be expected to have a similar electronic structure. To test whether the isolated doping of PTO by Pd results in the appearance of a magnetic moment in the system, we consider a $2 \times 2 \times 2$ supercell of PTO where a Pd atom substitutes either a Pb or Ti atom (see insets in Fig. 7). Figures 7(a) and

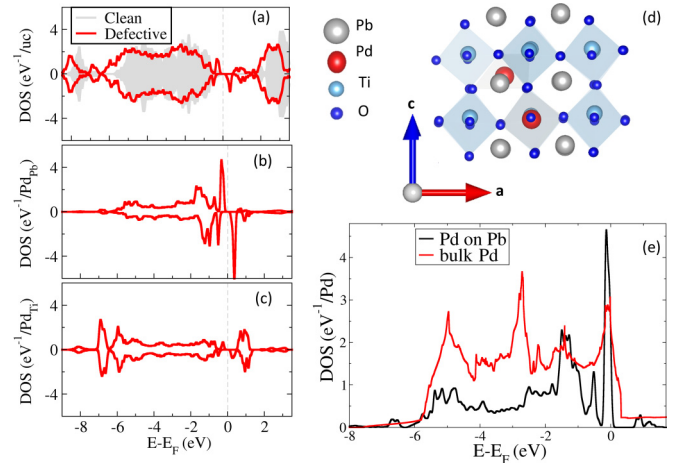


FIG. 8. (a) Spin-resolved DOS of clean (gray background) and defective (red curves) PbTiO_3 with two Pd atoms replacing Pb and Ti in a $2 \times 2 \times 2$ PbTiO_3 supercell along the $[111]$ direction [shown in (d)]. Positive (negative) DOS indicates majority- (minority-) spin contributions. The Fermi energy is shown by the dashed line. The DOS projected to Pd replacing Pb (b) and Ti (c), indicating a significant exchange splitting of the spin bands. (e) Paramagnetic DOS for bulk Pd (red curve) and Pd on Pb and Ti (black curve), indicating the enhancement of DOS at the Fermi energy for the latter.

7(c) show the total density of states (DOS) of the Pd-doped PTO (red curves) when a Pd atom substitutes Ti or Pb atoms, respectively, in comparison to the DOS of the bulk PTO [gray background in Figs. 7(a) and 7(c)]. Figures 7(b) and 7(d) show the DOS projected to the Pd atom on the Ti (Pb) site. It is evident that in both cases the induced defect states lie in the conduction and valence bands with no occupied defect states in the band gap of PTO. This indicates that the Pd on the Pb (Ti) site behaves as an isoelectronic substitution and the system remains insulating and nonmagnetic.

Next, we consider doping PbTiO_3 with a large concentration of Pd as in the experiment. To model this, we replace two Ti or Pb cations that are first or second nearest neighbors with Pd in the $2 \times 2 \times 2$ cubic supercell. Out of many ways to distributing two Pd atoms in the supercell, only when Pd replaces nearby Ti and Pb atoms along the $[111]$ direction, as shown in Fig. 8(d), does the magnetic moment of $\sim 2\mu_B$ appear in the case of Pd replacing Pb. Figure 8(a) shows the DOS of the defective system containing Pd in nearby Ti and Pb site compared to the nondefective bulk system. In contrast to the isolated Pd substitution in the Pb and Ti sites [Fig. 7(a) and Fig. 7(c)], the defect states appear in the band gap of the bulk PTO. Figure 8(b) shows DOS projected to the Pd replacing Pb atom, which reveals a spin-split band that arises from the exchange splitting of a DOS peak at about 2.0 eV [Fig. 7(d)]. The majority-spin band holds approximately one additional electron, resulting in a magnetic moment of $\sim 1\mu_B/\text{Pd}$. The remaining $\sim 1\mu_B$ comes from the spin polarization of the oxygen atoms bonded to Pd replacing Pb. In contrast, the DOS projected to Pd; replacing Ti [Fig. 8(c)] shows almost no spin-polarization. The two electrons in the majority-spin bands can be thought of as donated by a nominally $4+$ Pd atom residing on a nominally $2+$ Pb atom producing magnetism.

The splitting of the defect state of Pd on the Pb site can be understood in terms of the Stoner model [62]. In Fig. 8(e), we compare DOS of the doped Pd on the Pb site in PTO with the bulk Pd and find that the paramagnetic DOS of Pd on the Pb site is enhanced by $\sim 65\%$. As a result, the Stoner criterion— $ID(E_F) > 1$, where I is a Stoner exchange parameter—is satisfied, which favors a magnetic state.

Energetically isolated replacement of Pd on the Pb site is more favorable compared to the Pd-doping Ti atoms. The calculated formation energy $\Delta H(D) = E(D) - E(\text{Clean}) + \mu_r - \mu_a$, where $E(D)$, $E(\text{clean})$ are the energy of defective and clean system and μ_r and μ_a are the energy of removed and added atoms of the Pd replacing Pb atom. (~ 2.5 eV) is much smaller than that (~ 8.7 eV) of Pd replacing the Ti atom. The difference between Pd replacing Pb and Ti is so large that the converse results from the larger cells would not change qualitative conclusions whenever atomic energy (sometimes referred to as chemical potential) remains the same. Additionally, we also calculated the defect pair binding energy,

$$\Delta E = \Delta H(\text{Defect pair}) - \sum \Delta H(\text{Individual defect}),$$

and found that when nearby Pb and Ti along the [110] direction are replaced by Pd, the binding energy is negative ($\Delta E \sim -0.2$ eV). However, such configurations are nonmagnetic. The magnetic configurations we found have a positive binding energy ($\Delta E = \sim 1.0$ eV). This indicates that the probability of forming such a magnetic Pd-Pd pair is small even when doped with a large concentration of Pd, which is consistent with the low magnetic signal found experimentally.

V. COMPUTATIONAL METHODS

The theoretical modeling was performed using density functional theory (DFT) within the projected augmented wave (PAW) method for the electron-ion potential [63] and the local density approximation (LDA) for exchange and correlation, as implemented in Vienna *Ab initio* Simulation Package (VASP) [64,65]. The calculations were carried out using kinetic energy cutoff of 340 eV and $6 \times 6 \times 6$ k-point mesh for Brillouin zone integration. We fully relaxed ionic coordinates with the force convergence limit of 0.001 eV/atom. In the calculations, we used a theoretical LDA lattice constant of FE PbTiO₃. Calculations within the LDA+ U method, including a modest $U = 3.0$ eV, yielded similar results.

For all Pd⁴⁺ at Ti⁴⁺ perovskite B sites, we find only a small magnetic moment of $0.1\mu_B$. But for some Pd⁴⁺ at Pb²⁺ sites, the system is predicted to be FM. In the latter calculation, the source of valence compensation is not explicitly given, but we assume that the Pd⁴⁺ at the Pb site is balanced by Pd²⁺ at the Ti⁴⁺ B site. Parenthetically, we note that a similar hypothesis has been made for our recent data on FE SnTiO₃, where a relaxor behavior is found and attributed to be due to Sn⁴⁺ at the A site and Sn²⁺ at the $Ti B$ site [66].

VI. CONCLUSIONS

A single phase-pure PZTP30 ME having tetragonal crystal structure with $P4mm$ symmetry was discovered for possible room-temperature multistates tunable logic and nonvolatile memory elements under external E and H fields. It possesses high ME coefficients ~ 0.36 mV/cm Oe at $H_m = 3$ kOe in a single-phase system suggesting a strong coupling between piezo- and magnetostriction at nanoscale. It displays room-temperature weak ferromagnetism, strong ferroelectricity, and strong ME coupling. We believe the origin of magnetism is due to mixed valence states of the Pd²⁺/Pd⁴⁺ in PZT matrix, and in particular the presence of Pd⁴⁺ at Pd²⁺ perovskite A sites, as confirmed by XPS and XRF studies experimentally and DFT models. A sharp FE-paraelectric phase transition is observed near $T = 569$ K in dielectric studies, well supported by thermal studies. The strong room-temperature ME coupling makes it a possible future alternative of BiFeO₃ with a strong possibility for real device applications. PdO and possibly PbPdO₂ are magnetic contaminant phases in our ceramic samples, but only at cryogenic temperatures, and are measured as $<1\%$ abundance. PbPd₂O₄ is also magnetic, with a monoclinic-tetragonal $I2/a$ to $I4(1)/a$ transition at $T = 240$ K [67], but it is metallic and centric and hence cannot contribute to ferroelectricity or magnetoelectricity. Additionally, no evidence of this phase was found in our samples.

ACKNOWLEDGMENTS

This paper had financial support from the U.S. Department of Energy's Experimental Program to Stimulate Competitive Research (DOE-EPSCOR) Grant No. FG02-08ER46526. S.K., D.K.P., and K.P. would like to acknowledge fellowships from the National Science Foundation (NSF) Grant No. EPS-01002410.

-
- [1] W. Eerenstein, N. D. Mathur, and J. F. Scott, *Nature* **442**, 759 (2006).
- [2] J. F. Scott, *Science* **315**, 954 (2007).
- [3] M. Bibes and A. Barthélémy, *Nat. Mater.* **7**, 425 (2008).
- [4] A. J. Freeman and H. Schmid, *Magnetoelectric Interaction Phenomena in Crystals* (Gordon and Breach, London, 1975).
- [5] Y. Tokunaga, N. Furukawa, H. Sakai, Y. Taguchi, T.-h. Arima, and Y. Tokura, *Nat. Mater.* **8**, 558 (2009).
- [6] S.-W. Cheong and M. Mostovoy, *Nat. Mater.* **6**, 13 (2007).
- [7] I. Zutíć, J. Fabian, and S. Das Sarma, *Rev. Mod. Phys.* **76**, 323 (2004).
- [8] T. Kimura, T. Goto, H. Shintani, K. Ishizaka, T. Arima, and Y. Tokura, *Nature* **426**, 55 (2003).
- [9] D. A. Sanchez, N. Ortega, A. Kumar, R. S. Katiyar, and J. F. Scott, *AIP Adv.* **1**, 042169 (2011).
- [10] D. M. Evans, M. Alex, A. Schilling, A. Kumar, D. Sanchez, N. Ortega, R. S. Katiyar, J. F. Scott, and J. M. Gregg, *Adv. Mat.* **27**, 6068 (2015).
- [11] A. Kumar, I. Rivera, R. S. Katiyar, and J. F. Scott, *Appl. Phys. Lett.* **92**, 132913 (2008).
- [12] J. Wang, J. B. Neaton, H. Zheng, V. Nagarajan, S. B. Ogale, B. Liu, D. Viehland, V. Vaithyanathan, D. G. Schlom, U. V.

- Waghmare, N. A. Spaldin, K. M. Rabe, M. Wuttig, and R. Ramesh, *Science* **299**, 1719 (2003).
- [13] S. Goswami, D. Bhattacharya, L. Keeney, T. Maity, S. D. Kaushik, V. Siruguri, G. C. Das, H. Yang, W. Li, C. Z. Gu, M. E. Pemble, and S. Roy, *Phys. Rev. B* **90**, 104402 (2014).
- [14] E. Jartych, T. Pikula, K. Kowal, J. Dzik, P. Guzdek, and D. Czekaj, *Nanoscale Res. Lett.* **11**, 234 (2016).
- [15] A. N. Guthrie and M. J. Copley, *Phys. Rev.* **38**, 360 (1938).
- [16] A. Obinata, Y. Hibino, D. Hayakawa, T. Koyama, K. Miwa, S. Ono, and D. Chiba, *Sci. Rep.* **5**, 14303 (2015).
- [17] M. Birsan, B. Fultz, and L. Anthony, *Phys. Rev. B* **55**, 11502 (1997).
- [18] O. Yamada, F. Ono, I. Nakai, H. Maruyama, K. Ohta, and M. Suzuki, *J. Magn. Magn. Mater.* **31–34**, 105 (1993).
- [19] D. Khomskii, *Physics* **2**, 20 (2009).
- [20] J. F. Scott, *NPG Asia Materials* **5**, e72 (2013).
- [21] N. A. Spaldin, S. W. Cheong, and R. Ramesh, *Phys. Today* **63**(10), 38 (2010).
- [22] A. Kumar, N. Ortega, S. Dussan, S. Kumari, D. Sanchez, J. F. Scott, and R. S. Katiyar, *Solid State Phenom.* **189**, 1 (2012).
- [23] D. K. Pradhan, V. S. Puli, S. Kumari, S. Sahoo, P. T. Das, K. Pradhan, D. K. Pradhan, J. F. Scott, and R. S. Katiyar, *J. Phys. Chem. C* **120**, 1936 (2016).
- [24] M. Correa, A. Kumar, S. Priya, R. S. Katiyar, and J. F. Scott, *Phys. Rev. B* **83**, 014302 (2011).
- [25] A. A. Bokov and S. M. Emelyanov, *Phys. Status Solidi B* **164**, K109 (1991).
- [26] B. B. Van Aken, T. T. M. Palstra, A. Filippetti, and N. A. Spaldin, *Nat. Mater.* **3**, 164 (2004).
- [27] R. Saha, A. Sundaresan, and C. N. R. Rao, *Mater. Horiz.* **1**, 20 (2014).
- [28] D. Lebeugle, D. Colson, A. Forget, M. Viret, P. Bonville, J. F. Marucco, and S. Fusil, *Phys. Rev. B* **76**, 024116 (2007).
- [29] S. Kumari, N. Ortega, A. Kumar, S. P. Pavunny, J. W. Hubbard, C. Rinaldi, G. Srinivasan, J. F. Scott, and R. S. Katiyar, *J. Appl. Phys.* **117**, 114102 (2015).
- [30] S. Kumari, N. Ortega, A. Kumar, and R. S. Katiyar, *MRS Proceedings* (Materials Research Society, Boston, MA, 2014).
- [31] M. Fiebig, *J. Phys. D: Appl. Phys.* **38**, R123 (2005).
- [32] W. Prellier, M. P. Singh, and P. Murugavel, *J. Phys. Condens. Matter.* **17**, R803 (2005).
- [33] S. Picozzi and C. Ederer, *J. Phys. Condens. Matter.* **21**, 303201 (2009).
- [34] V. Garcia, M. Bibes, L. Bocher, S. Valencia, F. Kronast, A. Crassous, X. Moya, S. Enouz-Vedrenne, A. Gloter, D. Imhoff, C. Deranlot, N. D. Mathur, S. Fusil, K. Bouzehouane, and A. Barthélémy, *Science* **327**, 1106 (2010).
- [35] W. Wang, J. Zhao, W. Wang, Z. Gai, N. Balke, M. Chi, H. N. Lee, W. Tian, L. Zhu, X. Cheng, D. J. Keavney, J. Yi, T. Z. Ward, P. C. Snijders, H. M. Christen, W. Wu, J. Shen, and X. Xu, *Phys. Rev. Lett.* **110**, 237601 (2013).
- [36] R. Saha, A. Shireen, S. N. Shirodkar, M. S. Singh, U. V. Waghmare, A. Sundaresan, and C. N. R. Rao, *Inorg. Chem.* **50**, 9527 (2011).
- [37] K. M. Satyalakshmi, M. Alexe, A. Pignolet, N. D. Zakharov, C. Harnagea, S. Senz, and D. Hesse, *Appl. Phys. Lett.* **74**, 603 (1999).
- [38] S. Mukherjee, A. Roy, S. Auluck, R. Prasad, R. Gupta, and A. Garg, *Phys. Rev. Lett.* **111**, 087601 (2013).
- [39] H. M. Jang, S.-W. Song, K.-S. Lee, Y. S. Son, R. Gupta, A. Garg, J. Ratanapreechachai, and J. F. Scott, (npg) *Asia Mater.* **8**, e42 (2016).
- [40] D. I. Woodward, J. Knudsen, and I. M. Reaney, *Phys. Rev. B* **72**, 104110 (2005).
- [41] J. W. Bennett, I. Grinberg, P. K. Davies, and A. M. Rappe, *Phys. Rev. B* **82**, 184106 (2010).
- [42] J. Xue, D. Wan, and J. Wang, *Mater. Lett.* **39**, 364 (1999).
- [43] G. Srinivasan, E. T. Rasmussen, J. Gallegos, R. Srinivasan, Y. I. Bokhan, and V. M. Laletin, *Phys. Rev. B* **64**, 214408 (2001).
- [44] J. Joseph, T. M. Vimala, V. Sivasubramanian, and V. R. K. Murthy, *J. Mater. Sci.* **35**, 1571 (2000).
- [45] D. Walker, P. A. Thomas, and S. P. Collins, *Phys. Status Solidi A* **206**, 1799 (2009).
- [46] A. Baylet, P. Marécot, D. Duprez, P. Castellazzi, G. Groppi, and P. Forzatti, *Phys. Chem. Chem. Phys.* **13**, 4607 (2011).
- [47] O. Madelung, U. Rössler, and M. Schulz, *PdO: Magnetic Properties* (Landolt-Börnstein - Group III Condensed Matter 41D, Springer-Verlag, Berlin, 2000).
- [48] K. J. Lee, S. M. Choo, Y. Saiga, T. Takabatake, and M.-H. Jung, *J. Appl. Phys.* **109**, 07C316 (2011).
- [49] See Supplemental Material at <http://link.aps.org/supplemental/10.1103/PhysRevB.95.214109> for further details of XRD, XRF, EDS, XPS, and magnetic measurements.
- [50] S. Kumari, N. Ortega, D. K. Pradhan, A. Kumar, J. F. Scott, and R. S. Katiyar, *J. Appl. Phys.* **118**, 184103 (2015).
- [51] S. Kumari, N. Ortega, A. Kumar, J. F. Scott, and R. S. Katiyar, *AIP Advances* **4**, 037101 (2014).
- [52] L. S. Kibis, A. I. Stadnichenko, S. V. Koscheev, V. I. Zaikovskii, and A. I. Boronin, *J. Phys. Chem. C* **116**, 19342 (2012).
- [53] J.-N. Kim, K.-S. Shin, D.-H. Kim, B.-O. Park, N.-K. Kim, and S.-H. Cho, *Appl. Surf. Sci.* **206**, 119 (2003).
- [54] C. D. Wagner, W. M. Riggs, L. E. Davis, J. F. Moulder, and G. E. Muilenberg, *Handbook of X-ray Photoelectron Spectroscopy* (Perkin-Elmer Corp., Physical Electronics Division, Eden Prairie, Minnesota, 1979).
- [55] J. He, X. Lu, W. Zhu, Y. Hou, R. Ti, F. Huang, X. Lu, T. Xu, J. Su, and J. Zhu, *Appl. Phys. Lett.* **107**, 012409 (2015).
- [56] G. H. Khorrami, A. K. Zak, and S. M. Banihashemian, *Adv. Powder Technol.* **25**, 1319 (2014).
- [57] G. Arya, R. K. Kotnala, and N. S. Negi, *J. Am. Ceram. Soc.* **97**, 1475 (2014).
- [58] G. Harshe, J. P. Dougherty, and R. E. Newnham, *Int. J. Appl. Electromag. Mater.* **4**, 145 (1993).
- [59] M. Avellaneda and G. Harshe, *J. Intell. Mater. Sys. Struc.* **5**, 501 (1994).
- [60] C. W. Nan, S. X. Dong, D. Viehland, and G. Srinivasan, *J. Appl. Phys.* **103**, 031101 (2008).
- [61] V. M. Laletin and G. Srinivasan, *Ferroelectrics* **280**, 177 (2002).
- [62] E. C. Stoner, *Proc. R. Soc. London, Ser. A* **165**, 372 (1938).
- [63] P. E. Blöchl, *Phys. Rev. B* **50**, 17953 (1994).
- [64] G. Kresse and D. Joubert, *Phys. Rev. B* **59**, 1758 (1999).
- [65] G. Kresse and J. Furthmüller, *Phys. Rev. B* **54**, 11169 (1996).
- [66] J. Neugebauer and M. Scheffler, *Phys. Rev. B* **46**, 16067 (1992).
- [67] W. Yi, Y. Matsushita, M. Tanaka, and A. A. Belik, *Inorg. Chem.* **51**, 7650 (2012).